

Closing the loop: Autonomous experiments enabled by machine-learning-based online data analysis in synchrotron beamline environments

LINUS PITHAN,^{a*} VLADIMIR STAROSTIN,^a DAVID MAREČEK,^b
LUKAS PETERSDORF,^c CONSTANTIN VÖLTER,^a VALENTIN MUNTEANU,^a
MACIEJ JANKOWSKI,^d OLEG KONOVALOV,^d ALEXANDER GERLACH,^a
ALEXANDER HINDERHOFER,^a BRIDGET MURPHY,^c STEFAN KOWARIK^{b*} AND
FRANK SCHREIBER ^{a*}

^a*Universität Tübingen, Inst. für Angewandte Physik, Auf der Morgenstelle 10, 72076 Tübingen, Germany,* ^b*Universität Graz, Physikalische und Theoretische Chemie, Heinrichstraße 28, 8010 Graz, Austria,* ^c*Universität Kiel, Inst. für Experimentelle und Angewandte Physik, Leibnizstraße 19, 24118 Kiel, Germany,* and ^d*ESRF, The European Synchrotron, 71 avenue des Martyrs, CS 40220, 38043 Grenoble Cedex 9, France.* E-mail: linus.pithan@uni-tuebingen.de, stefan.kowarik@uni-graz.at, frank.schreiber@uni-tuebingen.de

machine learning; reflectometry; autonomous experiments; beamline control; XRR; NR; closed loop control; synchrotron

Abstract

Recently, there has been significant interest in applying machine learning (ML) techniques to X-ray scattering experiments, which proves to be a valuable tool for enhancing research that involves large or rapidly generated datasets. ML allows for the automated interpretation of experimental results, particularly those obtained from synchrotron or neutron facilities. The speed at which ML models can process data presents an important opportunity to establish a closed-loop feedback system, enabling real-time decision-making based on online data analysis. In this study, we describe the incorporation of ML into a closed-loop workflow for X-ray reflectometry (XRR), using the growth of organic thin films as an example. Our focus lies on the beamline integration of ML-based online data analysis and closed-loop feedback. We present solutions that provide an elementary data analysis in real time during the experiment without introducing the additional software dependencies in the beamline control software environment. Our data demonstrates the accuracy and robustness of ML methods for analyzing XRR curves and Bragg reflections and its autonomous control over a vacuum deposition setup.

1. Introduction

X-ray user facilities are amongst the largest scientific data producers in the world (Yanxon *et al.*, 2023). While experiments performed at these facilities cover an extensive range of multi-disciplinary sciences, they typically share a common data generation pattern, namely precisely positioning a specimen in the path of the X-ray beam and recording data (e.g. radiation scattered by the sample) captured by dedicated detectors (e.g. diffraction, imaging, spectroscopy) further downstream. Recent advances in accelerator development such as fourth-generation synchrotron light sources (Raimondi, 2016) and innovative detector technology (e.g. higher acquisition rates and

larger area detector dimensions) lead to continuously increasing data volume of these datasets that are more and more difficult to handle. In fact, in order to manage acquisition, analysis and storage of these, specific solutions developed at the facilities (Guijarro *et al.*, 2018; Allan *et al.*, 2019; Novelli *et al.*, 2023) or in data-driven national and international collaborations, e.g. DAPHNE4NFDI (Barty *et al.*, 2023) or PaNOSC (Carboni, 2022; Panosc, 2023), have been put in place, addressing these challenges.

Through the described technological advances and newly deployed infrastructure at modern beamlines and facilities, the way experiments are performed changes significantly towards more and more data-intense and data-driven experiments, increasingly relying on machine learning (ML) based approaches for data analysis (Chen *et al.*, 2021; Hinderhofer *et al.*, 2023). While facility instruments used to be basically fully isolated systems, often posing complications for visiting facility users to integrate sample-environment related equipment or data sources into the beamline data acquisition system, this changes rapidly with the recent developments in many aspects. This process is generally encouraged as the value of freely available, complete, augmented and documented FAIR datasets (Wilkinson *et al.*, 2016; Scheffler *et al.*, 2022) is recognized. These datasets are specifically valuable for machine learning activities and enable novel, previously impossible experiments that fully utilize modern infrastructure.

This paper introduces an approach for integrating real-time X-ray scattering and diffraction data analysis into a closed-loop control system that actively adjusts sample environment parameters. This approach unlocks exciting possibilities for conducting experiments using synchrotron radiation that unveil new insights into the underlying physics. We demonstrate the seamless integration of user-developed machine learning (ML) code with the beamline control infrastructure, enabling real-time data analysis.

Additionally, focusing on reflectometry as a case study, we provide a concise overview of a cutting-edge ML-based approach for predicting thin film parameters in both single-layer and multilayer structures.

2. Methods and Data

Several recent publications highlight the use of ML in synchrotron and neutron beamline environments (Noack *et al.*, 2021; Yager *et al.*, 2023; Beaucage & Martin, 2023; Szymanski *et al.*, 2023; Kandel *et al.*, 2023; Suzuki *et al.*, 2020; Hinderhofer *et al.*, 2023). These developments are mainly initiated at large-scale facilities or labs with privileged access rights that are necessary to integrate additional software code into beamline software environments. However, often user- and sample-specific ML techniques are needed in experiments. Therefore, this study explores potential approaches to deploy ML-based real-time analysis code at large scale facilities (X-ray and neutron sources) independent of the specific experiment or research facility. Where possible, we follow guidelines based on community initiatives such as PANOSC (Panosc, 2023), EXPANDS (Expands, 2023), DAPHNE4NFDI (Barty *et al.*, 2023) or MLExchange (Zhao *et al.*, 2022).

2.1. Software environments and structural requirements

Before discussing the architecture in detail, it is worth describing the complete data acquisition and handling process on a conceptual level. In the experiment described there are two main types of data generators: 1. the area detectors as counters (specifically a Dectris Pilatus 300k and a MaxiPix 2x2 with a CdTe sensor) controlled via LIMA (Petitdemange *et al.*, 2018), and 2. the motor positioners. Experiment control is performed via BLISS (Guijarro *et al.*, 2018) which also handles the saving of the collected data in the NeXus file format (using HDF5) (Könnecke *et al.*, 2015) and

triggers the ingestion of data and meta-data into the facility data portal.

The incorporation of user-developed code into the software environment of the beamline through software interfaces is crucial for the presented experiment, but also for many future experiments yet to come.

Software interfaces that enable the embedding of user-developed code into the beamline software environment are crucial for the presented experiment and - in our view - most likely also for many future experiments yet to come. To ensure operational stability of instruments with rapidly changing users there is an inherent dilemma from the facility point of view, since allowing modifications to the beamline's control software environment by one user puts the experiments of subsequent users at risk. Therefore, as a matter of best practice, well isolated software environments for beamline control and user code are crucial and one must find suitable methods to exchange data between these environments and software processes. From a practical point of view, such an approach also removes the burden of dealing with incompatibilities in software dependencies (e.g., versions of specific Python packages) that are used on both sides.

We identified different 'hooks' that typically exist in a modern beamline environment to achieve this inter-process communication between the beamline control software and user-supplied data analysis code, focusing on various levels of integration and portability between different light sources.

Modern beamline control systems, such as BLISS available at the ESRF (Guijarro *et al.*, 2018) and bluesky (Allan *et al.*, 2019), offer dedicated frameworks to access data in the beamline environment e.g. through "publishing" the data through an integrated in-memory database or via direct access to data- and event-streams produced by the acquisition process. Evidently, these are hooks which could be used to integrate online data analysis (see example in Supporting Information section SI-3), however these are usually tightly coupled to a specific facility and typically introduce a number of

critical dependencies into the user supplied code.

Another relatively simple option for external users to handle and test prior to the experiment, is to integrate on the level of the SCADA (supervisory control and data acquisition) used at the respective facility. The two most spread systems in this field are TANGO controls (Götz *et al.*, 2022; Tango, 2023) or EPICS (Epics, 2023). In the context of this study, we evaluated the integration via TANGO that is predominantly used at several European synchrotron facilities such as ESRF, DESY, SOLEIL or ALBA. Data transfer from the beamline control system via the available SCADA system forms part of the most common operations performed on the control system level and thus does not induce any additional software dependencies for the beamline control software environment.

As a third option, there is also the possibility to rely on workflow engines offered by the facilities (Nolf *et al.*, 2022). However, care must be taken with respect to the real-time capabilities of these systems, since they inherently rely on queue systems (job schedulers for batch processing) and thus may introduce additional delays under heavy load.

When it comes specifically to ML/AI pipelines/workflows, there is also potential to rely on standardized solutions that specifically fit the needs of handling larger ML models (e.g., NVIDIA Triton Inference Server) and thus abstract even beyond the specificity of beamline environments.

Evidently, combinations of all scenarios described above are possible and were partially evaluated in this work.

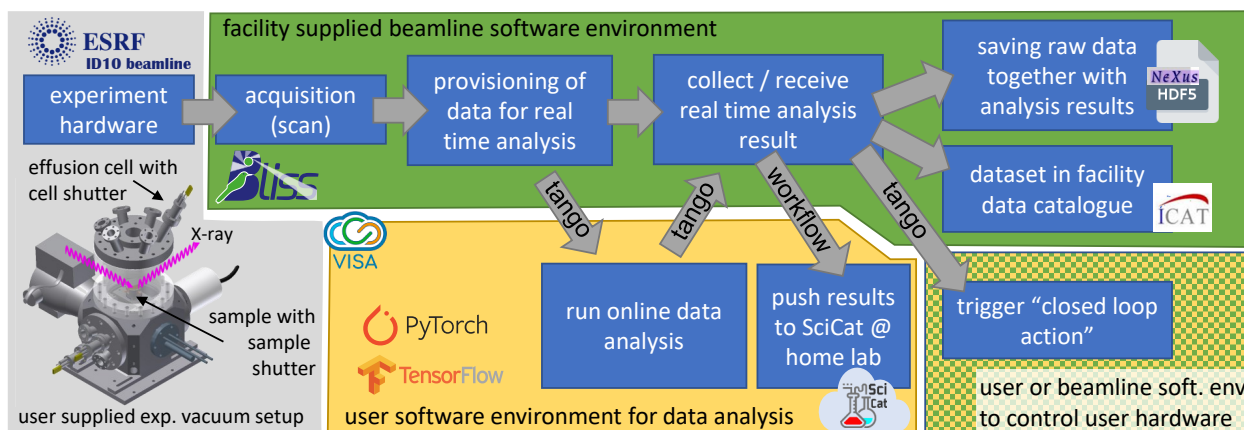


Fig. 1. Data flow during data collection, ML-based online data analysis and closed loop feedback. Data is collected using Bliss, transferred to online data analysis via tango and the analysis results are fed into closed-loop operation as well as saved together with raw data using Bliss again. Bottom left: experimental setup for molecular beam deposition.

2.2. Distributed online data analysis and closed-loop beamline integration

Splitting beamline control and ML based online data analysis in terms of infrastructure makes sense also when looking at the different hardware requirements of the two processes. While the beamline control process links to beamline instrumentation, it is physically tied to hardware that is available on the beamline itself. The ML data analysis process, which requires a powerful GPU, can also run on edge computing nodes (Babu *et al.*, 2022) or even in central computing facilities (Starostin *et al.*, 2022). For more integrated, routine solutions offered by the facilities themselves, edge computing is an attractive option in this context. Prioritizing the user's requirements, it is advantageous for a facility to offer infrastructure that is exclusively available to the particular user group performing the experiment. Through the collaborative efforts in the context of PANOSC the VISA system based on OpenStack (Visa, 2023) has been developed which essentially fulfills the needs described above.

Modern synchrotron beamlines are an ecosystem of distributed computing resources on their own. Therefore, a simple choice to establish communication between the beamline control software and the user-provided online data analysis resources is to rely on the beamline’s SCADA system (at ESRF: TANGO controls) for low dimensional data (sup. inf. sections A and B). Streaming options, however, become inevitable for high-rate, multidimensional data sources such as large area detector images.

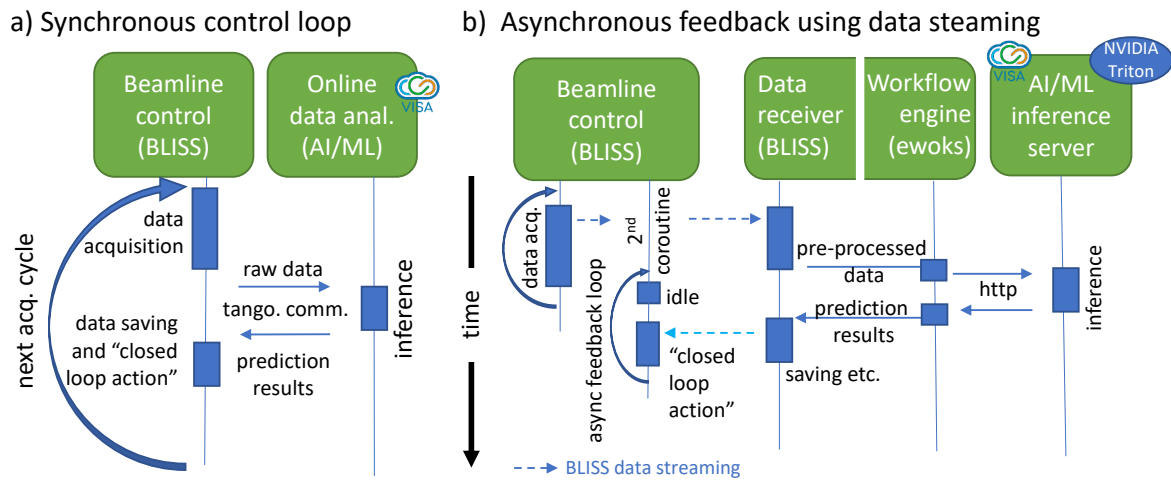


Fig. 2. Illustration of timing and architecture of implemented synchronous and asynchronous feedback loop. In a) data acquisition, ML inference and feedback action follow each other strictly in time (synchronous over distributed system) while in b) acquisition and data analysis + feedback are separated in independent coroutines to decouple independent processes. Further direct communication with the ML-model using TANGO controls is illustrated in a) while in b) an intermediate workflow system and an industrial inference server are used.

In Fig. 2 we illustrate the layout of two independently tested software configurations evaluated during the experiment presented. Fig. 2a) shows a fully *synchronous* acquisition and online analysis scheme relying on TANGO communication to transfer 1d data (binned ROI intensities extracted from detector images, here done via LIMA (Petitdemange *et al.*, 2018) to the online data analysis running on a user controlled virtual machine provisioned via VISA where the ML inference takes place. After pro-

cessing ML-results are made available in the main beamline control process and the ‘closed loop action’ can be triggered. Once completed, another acquisition starts (see pseudocode example in Supporting Information section Si-2).

Fig. 2b) shows a configuration that decouples the data acquisition and analysis+feedback into independent processes (asynchronous feedback) to maximize the data acquisition rates. Here, we use the streaming capabilities of BLISS to transfer reflectometry profiles into a workflow engine available at the beamline which in turn can communicate directly with an industrial AI inference server (here *Nvidia Triton* deployed on VISA hardware).

We emphasize again that for both described schemes no additional software needs to be installed into the beamline control software environment. The first, TANGO-based, approach largely benefits from the independence regarding the specific beamline control software solution and therefore its transferability to other facilities with a TANGO support layer on beamlines (e.g. DESY, SOLEIL or ALBA). Using industrial AI inference server in the second approach instead targets the use of standardized API interfaces commonly used in ML/AI.

2.3. Machine learning methods

While the focus of the present paper is not on the specific details of ML methods for X-ray data analysis, we briefly outline the concepts employed. For further details we refer to (Greco *et al.*, 2019; Greco *et al.*, 2021; Greco *et al.*, 2022; Mareček *et al.*, 2022; Munteanu *et al.*, 2023). For fast automated analysis of the measured XRR and Bragg reflection data, we rely on neural network-based maximum likelihood estimation (MLE). Compared to previous implementations, here we incorporate prior knowledge about the sample at a given time into the machine learning pipeline, thereby effectively mitigating uncertainty and constricting the range of potential solutions. For

a comprehensive, detailed discussion of this approach, see (Munteanu *et al.*, 2023).

The reflectometry analysis aims at reconstructing the scattering length density (SLD) profile of the studied sample based on the measured reflectivity curve. Given an SLD profile, the corresponding theoretical curve can be swiftly calculated (Parratt, 1954). However, reversing this operation presents a challenge because of the inherent ambiguity that often allows for multiple, different SLD profiles to correspond to the same curve within the bounds of measurement uncertainty. Fundamentally, this is related to the famous phase problem of scattering (since only the intensity, but not the phase is recorded in the detector). Consequently, it is vital in reflectivity analysis to make use of the physical understanding of the investigated system in order to reduce the number of potential solutions and identify the correct one. In previous ML-based works with two-layered structures (Greco *et al.*, 2019; Hinderhofer *et al.*, 2023), we approached this task by effectively fixing most of the parameters characterizing the SLD profile and training the neural network to estimate only the three unfixed parameters - thickness, roughness, and density of the top organic layer - anticipated to vary among the samples under study, with parameters of the silicon substrate with a silica top layer held constant. Expanding this method to accommodate a larger set of variable parameters, further techniques to address the ambiguity problem are needed (Munteanu *et al.*, 2023). In the present study, we build upon this approach and showcase two potential methods for integrating physical knowledge into the machine learning framework.

First, we propose to include the boundaries of the open parameters as an additional input to the neural network. As before, for each open parameter θ_i we designate broad ranges $[\theta_i^{total\ min}, \theta_i^{total\ max}]$ that determine the general scope of the neural network. Yet, in conjunction with these fixed ranges, we introduce *sample-dependent* ranges $[\theta_i^{\min}, \theta_i^{\max}]$ ($\theta_i^{\min} \leq \theta_i^{\max}; \theta_i^{\min}, \theta_i^{\max} \in [\theta_i^{total\ min}, \theta_i^{total\ max}]$) that impose constraints

on the fitted parameters for each sample studied and are supplied as additional input to the neural network alongside the measured curve. This method effectively confines the solution space for a particular sample while maintaining extensive overall parameter ranges within a single neural network. In instances where a single solution exists within the provided sample-dependent boundaries, the inverse operation becomes well-defined, enabling a precise fit. We note that this approach effectively combines the best of the two worlds: the flexibility of the parameter ranges of the conventional differential evolution method, and the speed of the neural network. Furthermore, for the real-time *in situ* analysis, it allows harvesting the information from the previous fits, as prior knowledge, so that the analysis of curves measured at different times for the same sample are no longer independent. For instance, during the growth experiment, we define the sample-dependent constraints on the growing film thickness based on the obtained result from a previous fit. This way, we leverage the physical understanding of the growth process (thickness of the growing layer cannot decrease over time) and the experimental setup (thickness cannot increase too rapidly), without a specific growth model restriction as used in (Mareček *et al.*, 2022).

The second method for integrating physical knowledge into the ML framework that we employ in this work is physics-based parameterization. In the case of ML-based reflectivity analysis, this approach was first introduced by (Mareček *et al.*, 2022), where the physics-based growth model allows to effectively reduce the number of estimated parameters. In this work, we apply this approach to the case of periodic multilayer structures by implementing a physics-based parametrization of the SLD profile. The standard parameterization of the box model implies three parameters (or four parameters when including absorption) per single layer for each box (density, thickness, roughness). Given that a single molecular monolayer block is typically modeled by two layers, such parameterization would require up to $2 \cdot 30 \cdot 3 = 180$ independently

fitted parameters (when considering 30 monolayers) resulting in a \mathbb{R}^{180} solution space. However, such parameters are largely correlated, because the monolayers consist of the same material, feature the same thickness, etc. To provide this information to the neural network, we introduce a set of 17 independently fitted or predicted parameters, that together define all the 180 parameters of the box model. Such parameterization is based on a physical understanding of monolayer structures and significantly decreases the task's complexity (Mareček *et al.*, 2022). The parametrization is illustrated in Fig. 3 and is discussed in more detail in (Munteanu *et al.*, 2023).

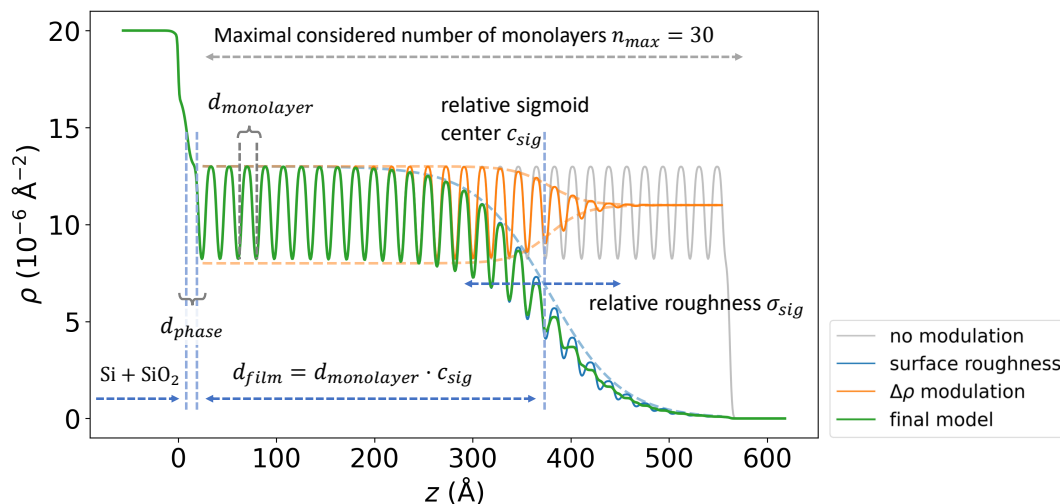


Fig. 3. Parameterization of the periodic multilayer structure. The stacked layers share the same thickness $d_{\text{monolayer}}$, roughnesses, and SLD densities. Most of the parameters introduced are relative to $d_{\text{monolayer}}$. Two sigmoid functions modulate the resulting periodic SLD profile. The position of the first sigmoid c_{sig} defines the number of monolayers and the corresponding thickness $d_{\text{film}} = d_{\text{monolayer}} \cdot c_{\text{sig}}$, while its width σ_{sig} determines the surface roughness $\sigma_{\text{film}} = \sigma_{\text{sig}} \cdot d_{\text{monolayer}}$. The second sigmoid modulates the contrast $\Delta\rho$ between the layers, resulting in smoother SLD profile at the surface.

We have developed a fast, GPU-accelerated module within the PyTorch framework that calculates reflectivity curves in order to train the neural networks utilized in the experiment in real-time during the beamtime. This module seamlessly integrates into

the training process, enabling on-the-fly XRR simulations throughout the training phase. Consequently, we were able to quickly adjust the training settings (even during the beamtime), eliminating the requirement for meticulous pre-planning. Note, that we rely on preprocessing operations and the rich postprocessing pipeline introduced in (Greco *et al.*, 2021; Greco *et al.*, 2022) that features q offset sampling and LMS fit. A major addition to the postprocessing step of the previous works is the introduction of a new optional fitted parameter that models a linear change of thickness *during the measurement of a single curve* as we perform *in situ* and real-time experiments. Therefore, for a single scan, we take into account the time-dependent layer thickness $d(t)$ and the time-dependent incidence angle corresponding to momentum transfer $q(t)$. Together with other time-independent parameters θ , $d(t)$ and $q(t)$ define the curve: $R = R(q(t), d(t), \theta)$. A linear model of a growth process $d(t) = d_0 + t \frac{\Delta d}{\Delta t}$ is a very good approximation for the short duration of a quick real-time scan. Consequently, we fit two parameters d_0 and $\frac{\Delta d}{\Delta t}$ for each curve via LMS, using the neural network prediction as an initial guess for the parameter d_0 . The introduction of this time-dependent parameter is required to accurately fit XRR curves measured during the growth in the case of a fast growth process relative to the data acquisition time for a single XRR profile, as Kiessig fringes will be slightly narrower at high q as compared to low q .

2.4. Data handling

All data, including the extracted parameters of the online data analysis, have been stored in a fully correlated fashion, i.e. raw data alongside with analysis results in NeXus HDF5, and are publicly available through the ESRF data portal (Pithan *et al.*, 2023).

Using the ESRF file-saving infrastructure (Bliss + NeXusWriter) enabled the vis-

iting experimentalists to directly insert the online data analysis results into the data files published by the beamline (see supporting information for details). Furthermore, through integrating into the ESRF beamline software ecosystem, the online data analysis results could seamlessly be transferred into the accompanying electronic logbook, allowing a first overview of the experimental results ordered via timestamps.

2.5. Experiment

This study has been performed on the surface scattering branch of the ESRF ID10 beamline (Jankowski *et al.*, 2023). A beam energy of 17.0keV and beamsize of $30\times 30\mu\text{m}$ was used. We use X-ray reflectometry (XRR), an established surface scattering techniques, performed following standard procedures (Daillant & Gibaud, 2009; Tolan, 1999; Holý *et al.*, 1999; Seeck *et al.*, 2002). A user supplied UHV sample environment (Fig. 1) has been installed in horizontal geometry. Molecular thin film samples are prepared *in situ* using molecular beam deposition (Ritley *et al.*, 2001; Zykov *et al.*, 2017).

To achieve the objective of stabilizing and terminating the self-assembly, growth, and crystallization characteristics of molecular thin film studies *in situ*, a closed-loop control system has been implemented, leveraging the ML-based online analysis. This closed-loop control allows for autonomous experiments. In this particular study, the ML-based closed loop system assumes control over the operation of two shutters, which involves covering either the substrate or the incoming molecular beam (refer to Fig. 1). To limit beam damage, which might occur for longer scan times at lower deposition rates, we reduced the X-ray flux to a level where there was no noticeable impact on Bragg peak intensities over the time of a growth run at our deposition rates.

In this study, molecular thin films of aluminium-tris(8-hydroxyquinolin) (Alq_3 , $\text{C}_{27}\text{H}_{18}\text{AlN}_3\text{O}_3$), a frequently used component in organic light-emitting diodes, were

grown to serve as an exemplary material system for amorphous molecular thin films (Mondal *et al.*, 2021). To demonstrate the online capabilities regarding the analysis of crystalline multilayer systems the organic semiconductor N,N'-Dioctyl-3,4,9,10-perylendicarboximid (PTCDI-C₈, C₄₀H₄₂N₂O₄) (Zykov *et al.*, 2017; Krauss *et al.*, 2008) was chosen for demonstration purposes. For details on the scientific background of these materials, we refer to (Kowarik *et al.*, 2008; Schreiber, 2004; Witte & Wöll, 2004).

3. Results and discussion

To verify and test the technical solutions discussed above, we aim to grow molecular thin films of predefined thickness where the ML-based closed loop takes control over the termination of the growth process by closing the relevant deposition shutters. It became evident that it is crucial to provide prior knowledge about the film parameters (e.g. plausible film thickness ranges) as input of the ML-model to achieve robust fitting for a large number of consecutive scans. In this work priors were used to describe minimum and maximum boundaries for each parameter.

3.1. Discussion of ML in XRR and Bragg reflection fitting

To achieve good performance of ML predictions on XRR signals it is important to consider corrections such as q -shift (for slight misalignment) and subsequent fitting using a LMS algorithm as described in (Greco *et al.*, 2021). Furthermore, due to the *in situ* data-taking that is inherent to closed loop feedback, the varying film thickness during a single scan must be taken into account if the scan speed is not fast compared to the deposition speed. We accommodate this additional effect as an additional parameter in the subsequent LMS fit as discussed above (snippet in Supporting Information section SI-4). In both examples of amorphous and multilayer

thin films, prior information was taken into account for the online ML analysis result: In the multilayer fits physical knowledge was embedded in the parametrization of the electron density model and rather narrow training ranges of the ML model. In contrast, wide training ranges were used for the single-layer model, but prior information was taken into account by inputting it into the ML model to achieve a certain regularization of the results. Here, in the dataset presented in Fig. 4, through the use of priors, the expected film thickness was constrained to increase by at most 50 Å and decrease by no more than 25 Å for the ML based real-time analysis. This still gives the model sufficient flexibility to predict changes during the film growth, but imposes weak boundaries based on the scan speed and deposition rate.

3.2. Single layer fits (*Kiessig oscillations*)

In Fig. 4a we show exemplary reflectometry profiles acquired during thin film growth of Alq3 using continuous scans (also known as *flyscans* or *fastscans*) together with the corresponding ML results of layer parameters. As can be seen from the presented, footprint corrected scans, we achieved a very good fit quality using the ML-approach with priors. Both the period of Kiessig fringes as well as the roughness induced damping of Kiessig fringes are correctly reproduced in the ML fits. This is a prerequisite for achieving closed loop control to terminate growth at the target thickness, but due to the finite duration of the scans (45s per XRR profile in Fig. 4a) and an average growth rate of 1 nm/min, the target thickness may be reached during a scan. Therefore, we used a linear extrapolation of the thickness information of previous scans to automatically calculate the best moment to close the shutter, as yet another asynchronous process (see Supporting Information section SI-3). Fig. 4b shows the result of the closed loop deposition control for several target thicknesses between 80 Å and 640 Å. The target thicknesses are plotted on the x-axis, while the true film thick-

nesses at which the deposition was terminated are given on the y-axis. As expected for a functioning closed loop control, the data indeed falls on the diagonal line, except for one outlier. Overall, the chosen target thicknesses could be reached within $\pm 2\text{\AA}$ (0.1%) average accuracy.

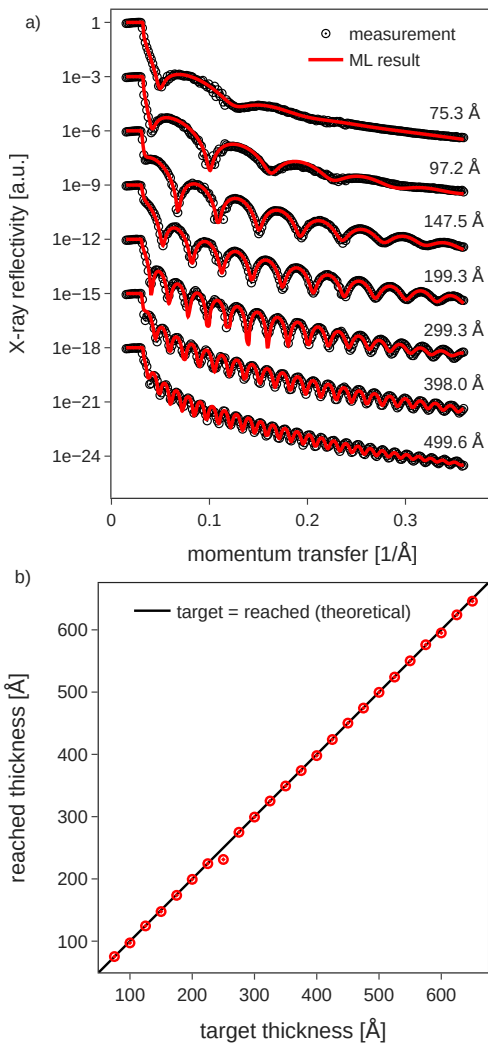


Fig. 4. ML controlled thin film deposition: a) Exemplary measurements and fits. The experimental data are acquired using fast, real-time scans, thus the poor counting statistics around $q \simeq 0.11/\text{\AA}$ is due to the limited number of absorber changes. b) target thicknesses in closed loop operation vs. actually measured thicknesses after the closed loop feedback terminated the growth.

3.3. Multilayer fits (Bragg reflections)

Not only amorphous thin film structures, but also multilayers of the molecule PTCDI-C₈ were studied. By incorporating physical knowledge of the sample structure into the parametrization of the used ML model we are able to fit Laue fringes and the molecular Bragg-peak that arises with increasing film thickness from molecular multilayers (Fig. 5a). To speed up data acquisition only a relatively short q -range centered around the molecular Bragg peak was repeatedly scanned while running in closed loop mode. An initial 'full' XRR curve, including the total reflection edge, was used for signal normalization before activating the closed loop operating mode.

Again, these scans around the Bragg reflection could be fitted by ML with high fidelity, reproducing the Bragg peak and the period of the Laue oscillations and their asymmetric intensity to the left and right of a Bragg reflection. The corresponding electron density profiles from the live fits are shown in Fig. 5b, from which one can directly infer the number of deposited monolayers, as one oscillation of the scattering length density corresponds to one PTCDI-C₈ monolayer. Comparing the film thickness from the ML fits of the Bragg region to the total thickness derived from a measurement of the deposition flux with a quartz crystal microbalance (QCM) one again finds reasonable agreement as shown in Fig. 6a). For thicknesses above 250 Å the agreement is good. Some scatter is visible below this thickness, even though the quality ML fit of the individual reflectometry curves is good (Fig. 6b)). This particular example shows the difficulty of ambiguous XRR fits, where several sample structure models can fit a single X-ray curve. Also, note, that the QCM measures total film thickness only if a constant sticking factor on the substrate and previously deposited molecular material is assumed. Further, the Laue oscillations do not correspond to the total film thickness, but the coherently ordered film thickness, so initial disorder in the crystal lattice may to some degree contribute to the observed deviations for low film

thicknesses (additionally, of course, the potentially non-integer layer occupancy during growth may interplay as well (Rieutord *et al.*, 1989)). Overall, we conclude that the ML results (live) of the coherent film thickness during data acquisition nicely match our detailed post growth analysis and yield consistent data for larger film thickness of our sample system. This, in principle, enables closed loop feedback e.g. to target growth of a fixed number of crystalline lattice planes in a thin film sample.

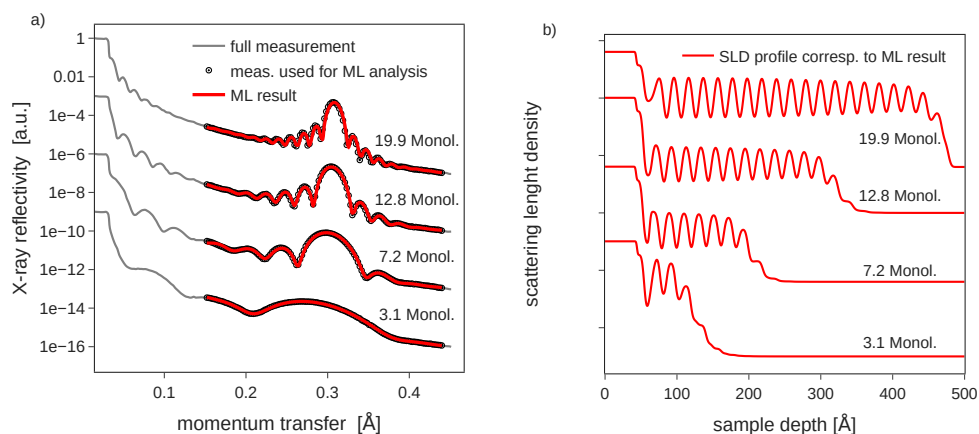


Fig. 5. a) ML-based fits of PTCDI- C_8 multilayer structures. As input for the ML-model only points measured around the PTCDI- C_8 Bragg-peak were taken into account to enable faster data acquisition. b) scattering length density profiles corresponding to a).

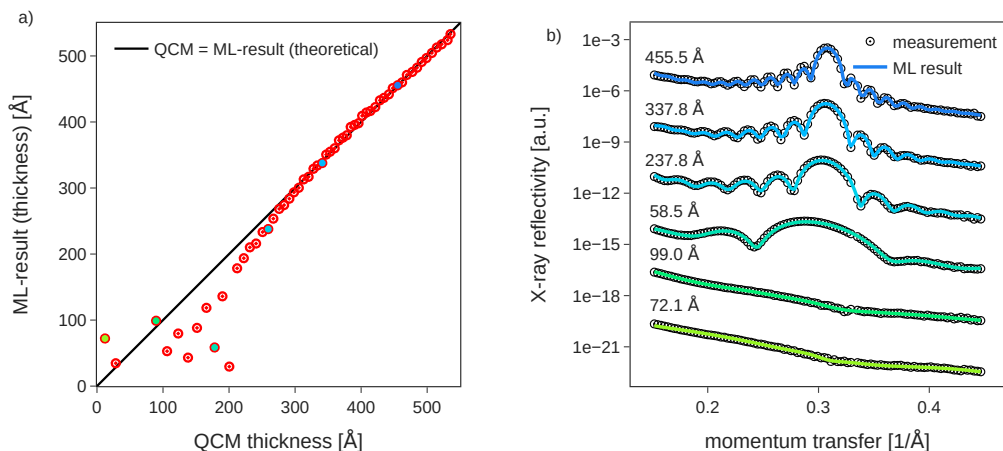


Fig. 6. a) Thin film thickness extracted through ML model in real time during the measurement compared to a quartz crystal micro balance (QCM) reference. For films with thickness above $\simeq 250$ Å, i.e. $\simeq 12$ mol. monolayers ML-results are reliable. b) selected fits from the real-time dataset. Ambiguity in the thickness predictions for lower thicknesses mainly results from the absence of significant features in the investigated q -range.

3.4. Robust feedback to control growth

Within the domain of ML-based closed-loop feedback, we emphasize the criticality of robust real-time analysis for successful operation. Especially in Fig. 4 the expected trend of increasing thickness from scan to scan during growth is clearly observed. The robustness of the ML results is especially important when facing the challenge on the control side that extracted parameters must be used to extrapolate the film thickness into the near future. Only robust fits can lead to a meaningful time-series, so that after extrapolation the autonomous growth termination can act at the moment the predefined film thickness is reached – which does not necessarily coincide with the end of a performed scan. In this study, the time resolution of the reflectivity measurements (repeat rate of scans) could be identified as the most critical bottleneck of the given setup. Therefore, the limited time resolution had to be addressed through an additional asynchronous process taking care of the temporal extrapolation and the

triggering of actions in close loop operation. Here BLISS is very well equipped for this kind of tasks through its tight integration of *gevent* to enable coroutine operation (Bilenko & Madden, 2023). Through averaging several of the last ML-results (a.k.a. “predictions”), isolated slight outliers in the ML results could be tolerated and were not sufficient to invalidate the live feedback mechanism. Overall, the 2% thickness error proves the robust ML fitting, extrapolation and closed loop feedback action.

3.5. Further integration potential

For the experiment conducted in the context of this work it was possible to store ML analysis results together with the original raw data and to interact with the facility-provided electronic logbook (ELN). However, ingesting machine-readable metadata into the facility data catalog remained difficult. In order to support and contribute to a thriving ecosystem of ML models for X-ray data analysis, i.e. physics-informed ML models and sample-system specific ML models, it is of crucial importance that facilities provide -ideally standardized- interfaces and best practice guidelines on how externally developed code should interact with the respective beamline control and data storage systems. Initiatives similar to DAPHNE4NFDI (Barty *et al.*, 2023) are well suited for discussion in this context, since they bring together facilities and the user community, including experienced users, to jointly design research data infrastructure along a process chain all the way from the proposal and experiment to the fully analyzed and archived data.

4. Conclusions and outlook

In this study we established a complete closed loop feedback cycle for controlling thin film and crystal growth exclusively relying on real-time scattering data and online ML analysis. The presented scheme is well suited for a broader range of *in situ* and

in operando experiments. Not only growth dynamics can be observed with X-rays, but also processes in dynamic equilibrium where the information extracted from the scattering data itself can be used to stabilize the equilibrium. Specifically, for XRR this may for instance involve control over various liquid systems with a Langmuir trough as one possibility to prepare environments (e.g. lipid bilayers) with precise surface pressure to have stable conditions at the liquid-air interface. Here the ML approach for feedback directly relates to the film properties measured with XRR, whereas of course the sample environment (e.g. surface pressure of a Langmuir trough) may also be controlled externally. In a broader picture, we see a bright future to embed ML based feedback loops also for other types of scattering experiments e.g. involving electrochemical control over battery charging or control over electrochemical sample environment conditions or catalytic conditions in experiments on nanoparticles. It also extends to other synchrotron-based techniques (Chen *et al.*, 2021; Hinderhofer *et al.*, 2023), as well as neutron-based techniques, including in particular neutron reflectometry (NR) (Treece *et al.*, 2019).

With the focus on publicly available FAIR datasets hosted in facility data catalogs we see the potential of ML based online data analysis in helping to make these datasets in catalogs “more fair and more reusable”. This is possible through enriching the currently archived raw dataset at least with the preliminary analysis results on the fly. Live ML X-ray data analysis has the ability to complete datasets with scientifically relevant machine-readable metadata as well as automated capture of scientific results in electronic logbooks (ELNs) accompanying the dataset in the facility data catalog. We are convinced that the presented approach can contribute significantly to a more efficient use of beamtime at large scale facilities. We envision that integration of live data analysis and feedback loops with ML models will become more established at beamlines along the lines presented here. Then, facility users can use ML to observe

live how experiments progress and also perform previously unattainable experiments with direct feedback and contribute to an ever-growing, meaningful X-ray dataset pool.

Appendix A

Data Availability Statement

The specific beamline integration python scripts as well as the TANGO server embedding the ML model used in this study are available in the Supporting Information accompanying the published article. Data underlying this publication is available in the ESRF data repository (Pithan *et al.*, 2023). Experimental data used to prepare for the beamtime is available in (Pithan *et al.*, 2022). A reference ML model is available in (Greco, 2022) and soon to be found in (Munteanu *et al.*, 2023).

Appendix B

Acknowledgements

We acknowledge the European Synchrotron Radiation Facility (ESRF) for providing of synchrotron radiation at the ID10 beamline. Further, we express our gratitude to those offering support with the ESRF computing infrastructure, especially Jean-Francois Perrin, Wout de Nolf, Samuel Debionne and Valentin Valls.

We also acknowledge financial support via the DAPHNE4NFDI project and the BMBF.

Appendix C

Glossary

BLISS	ESRF experiment control system https://gitlab.esrf.fr/bliss/bliss
LIMA	LImA : Library for Image Acquisition (ESRF) https://lima1.readthedocs.io
SCADA	supervisory control and data acquisition system
TANGO	SCADA system originally developed at the ESRF https://www.tango-controls.org

References

- Allan, D., Caswell, T., Campbell, S. & Rakinin, M. (2019). *Synchrotron Radiation News*, **32**(3), 19–22.
10.1080/08940886.2019.1608121
- Babu, A. V., Zhou, T., Kandel, S., Bicer, T., Liu, Z., Judge, W., Ching, D. J., Jiang, Y., Veseli, S., Henke, S., Chard, R., Yao, Y., Sirazitdinova, E., Gupta, G., Holt, M. V., Foster, I. T., Miceli, A. & Cherukara, M. J. (2022). Publisher: arXiv. DOI: 10.48550/ARXIV.2209.09408.
<https://arxiv.org/abs/2209.09408>
- Barty, A., Gutt, C., Lohstroh, W., Murphy, B., Schneidewind, A., Grunwaldt, J.-D., Schreiber, F., Busch, S., Unruh, T., Bussmann, M., Fangohr, H., Görzig, H., Houben, A., Kluge, T., Manke, I., Lützenkirchen-Hecht, D., Schneider, T. R., Weber, F., Bruno, G., Einsle, O., Felder, C., Herzig, E. M., Konrad, U., Markötter, H., Rossnagel, K., Sheppard, T. & Turchinovich, D. (2023). DAPHNE4NFDI - Consortium Proposal. DOI: 10.5281/ZENODO.8040606.
<https://zenodo.org/record/8040606>
- Beaucage, P. A. & Martin, T. B. (2023). *Chemistry of Materials*, **35**(3), 846–852.
10.1021/acs.chemmater.2c03118
- Bilenko, D. & Madden, J. (2023). gevent.
<http://www.gevent.org/>
- Carboni, N. (2022). PaNOSC key achievements. DOI: 10.5281/ZENODO.7347537.
<https://zenodo.org/record/7347537>
- Chen, Z., Andrejevic, N., Drucker, N. C., Nguyen, T., Xian, R. P., Smidt, T., Wang, Y., Ernstorfer, R., Tennant, D. A., Chan, M. & Li, M. (2021). *Chemical Physics Reviews*, **2**(3), 031301.
10.1063/5.0049111
- Daillant, J. & Gibaud, A. (eds.) (2009). *X-ray and neutron reflectivity: principles and applications*. No. 770 in Lecture notes in physics. Berlin: Springer, 2nd ed. OCLC: ocn261955200.
- Epics (2023). EPICS controls.
<https://epics-controls.org/>
- Expands (2023). DOI: 10.3030/857641.
<https://expands.eu/>
- Greco, A. (2022). mlreflect: v0.21.0. DOI: 10.5281/zenodo.6467047.
<https://zenodo.org/record/6467048>
- Greco, A., Starostin, V., Edel, E., Munteanu, V., Rußegger, N., Dax, I., Shen, C., Bertram, F., Hinderhofer, A., Gerlach, A. & Schreiber, F. (2022). *Journal of Applied Crystallography*, **55**(2), 362–369.
10.1107/S1600576722002230
- Greco, A., Starostin, V., Hinderhofer, A., Gerlach, A., Skoda, M. W. A., Kowarik, S. & Schreiber, F. (2021). *Machine Learning: Science and Technology*, **2**(4), 045003.
10.1088/2632-2153/abf9b1

- Greco, A., Starostin, V., Karapanagiotis, C., Hinderhofer, A., Gerlach, A., Pithan, L., Liehr, S., Schreiber, F. & Kowarik, S. (2019). *Journal of Applied Crystallography*, **52**(6), 1342–1347.
10.1107/S1600576719013311
- Guijarro, M., Beteva, A., Coutinho, T., Dominguez, M.-C., Guilloud, C., Homs, A., Meyer, J., Michel, V., Papillon, E., Perez, M. & Petitdemange, S. (2018). *Proceedings of the 16th Int. Conf. on Accelerator and Large Experimental Control Systems*.
10.18429/JACOW-ICALEPCS2017-WEBPL05
- Götz, A., Abeillé, G., Bertrand, B., Bourtembourg, R., Brandl, G., Braun, T., Goryl, P., Hardion, V., Joubert, A., Lacoste, D., Leclercq, N., Liszcz, M., Pascual-Izarra, C., Pivetta, L., Rubio-Manrique, S. & Venter, A. (2022). *Proceedings of the 18th International Conference on Accelerator and Large Experimental Physics Control Systems*.
10.18429/JACOW-ICALEPCS2021-WEAR01
- Hinderhofer, A., Greco, A., Starostin, V., Munteanu, V., Pithan, L., Gerlach, A. & Schreiber, F. (2023). *Journal of Applied Crystallography*, **56**(1), 3–11.
10.1107/S1600576722011566
- Holý, V., Pietsch, U. & Baumbach, T. (1999). *High-resolution X-ray scattering from thin films and multilayers*. No. v. 149 in Springer tracts in modern physics. Berlin ; New York: Springer.
- Jankowski, M., Belova, V., Chushkin, Y., Zontone, F., Levantino, M., Narayanan, T., Konovalov, O. & Pastore, A. (2023). *Nuclear Instruments and Methods in Physics Research Section B: Beam Interactions with Materials and Atoms*, **538**, 164–172.
10.1016/j.nimb.2023.02.034
- Kandel, S., Zhou, T., Babu, A. V., Di, Z., Li, X., Ma, X., Holt, M., Miceli, A., Phatak, C. & Cherukara, M. (2023). DOI: 10.48550/ARXIV.2301.05286.
<https://arxiv.org/abs/2301.05286>
- Kowarik, S., Gerlach, A. & Schreiber, F. (2008). *Journal of Physics: Condensed Matter*, **20**(18), 184005.
10.1088/0953-8984/20/18/184005
- Krauss, T. N., Barrena, E., Zhang, X. N., De Oteyza, D. G., Major, J., Dehm, V., Würthner, F., Cavalcanti, L. P. & Dosch, H. (2008). *Langmuir*, **24**(22), 12742–12744.
10.1021/la8030182
- Könnecke, M., Akeroyd, F. A., Bernstein, H. J., Brewster, A. S., Campbell, S. I., Clausen, B., Cottrell, S., Hoffmann, J. U., Jemian, P. R., Männicke, D., Osborn, R., Peterson, P. F., Richter, T., Suzuki, J., Watts, B., Wintersberger, E. & Wuttke, J. (2015). *Journal of Applied Crystallography*, **48**(1), 301–305.
10.1107/S1600576714027575
- Mareček, D., Oberreiter, J., Nelson, A. & Kowarik, S. (2022). *Journal of Applied Crystallography*, **55**(5), 1305–1313.
10.1107/S1600576722008056
- Mondal, K. P., Bera, S., Gupta, A., Kumar, D., Gome, A., Reddy, V. R., Ito, N., Yamada-Takamura, Y., Pandit, P. & Roth, S. V. (2021). *Journal of Physics D: Applied Physics*, **54**(15), 155304.
10.1088/1361-6463/abd9eb
- Munteanu, V., Starostin, V., Greco, A., Pithan, L., Gerlach, A., Hinderhofer, A., Kowarik, S. & Schreiber, F. (2023). (in preparation) Neural network analysis of neutron and X-ray reflectivity data: incorporating prior knowledge for tackling the phase problem.
- Noack, M. M., Zwart, P. H., Ushizima, D. M., Fukuto, M., Yager, K. G., Elbert, K. C., Murray, C. B., Stein, A., Doerk, G. S., Tsai, E. H. R., Li, R., Freychet, G., Zhernenkov, M., Holman, H.-Y. N., Lee, S., Chen, L., Rotenberg, E., Weber, T., Goc, Y. L., Boehm, M., Steffens, P., Mutti, P. & Sethian, J. A. (2021). *Nature Reviews Physics*, **3**(10), 685–697.
10.1038/s42254-021-00345-y
- Nolf, W. D., Payno, H., Svensson, O. & Koumoutsos, G. (2022). ewoks. DOI: 10.5281/ZENODO.6075053. <https://ewoks.readthedocs.io>.
<https://zenodo.org/record/6075053>

- Novelli, M., Egli, S., Minotti, C., Bolmsten, F., McReynolds, D., Pithan, L., Bliven, S., Leorato, M., Shemilt, L. & Richter, T. (2023). SciCat.
<https://scicatproject.github.io/>
- Panosoc (2023). DOI: 10.3030/823852.
<https://www.panosoc.eu/>
- Parratt, L. G. (1954). *Physical Review*, **95**(2), 359–369.
 10.1103/PhysRev.95.359
- Petitdemange, S., Claustre, L., Henry, A., Homs, A., Homs Regojo, R., Langlois, F., Mant, G., Naudet, D., Noureddine, A. & Papillon, E. (2018). *Proceedings of the 16th Int. Conf. on Accelerator and Large Experimental Control Systems*.
 10.18429/JACOW-ICALEPCS2017-TUPHA194
- Pithan, L., Greco, A., Hinderhofer, A., Gerlach, A., Kowarik, S., Rußegger, N., Dax, I. & Schreiber, F. (2022). Reflectometry curves (XRR and NR) and corresponding fits for machine learning. Dataset. Publisher Zenodo. DOI: 10.5281/zenodo.6497437.
<https://zenodo.org/record/6497438>
- Pithan, L., Starostin, V., Marecek, D., Petersdorf, L., Völter, C., Munteanu, V., Jankowski, M., Kononov, O., Gerlach, A., Hinderhofer, A., Murphy, B., Kowarik, S. & Schreiber, F. (2023). Controlled thin film growth through machine-learning based closed-loop feedback with online X-ray scattering analysis. Dataset. Publisher ESRF. DOI: 10.15151/ESRF-DC-1249105707.
<https://doi.esrf.fr/10.15151/ESRF-DC-1249105707>
- Raimondi, P. (2016). *Synchrotron Radiation News*, **29**(6), 8–15.
 10.1080/08940886.2016.1244462
- Rieutord, F., Benattar, J. J., Rivoira, R., Lepêtre, Y., Blot, C. & Luzet, D. (1989). *Acta Crystallographica Section A Foundations of Crystallography*, **45**(7), 445–453.
 10.1107/S0108767389001327
- Ritley, K. A., Krause, B., Schreiber, F. & Dosch, H. (2001). *Review of Scientific Instruments*, **72**(2), 1453.
 10.1063/1.1336822
- Scheffler, M., Aeschlimann, M., Albrecht, M., Bereau, T., Bungartz, H.-J., Felser, C., Greiner, M., Groß, A., Koch, C. T., Kremer, K., Nagel, W. E., Scheidgen, M., Wöll, C. & Draxl, C. (2022). *Nature*, **604**(7907), 635–642.
 10.1038/s41586-022-04501-x
- Schreiber, F. (2004). *physica status solidi (a)*, **201**(6), 1037–1054.
 10.1002/pssa.200404334
- Seeck, O. H., Kim, H., Lee, D. R., Shu, D., Kaendler, I. D., Basu, J. K. & Sinha, S. K. (2002). *Europhysics Letters (EPL)*, **60**(3), 376–382.
<https://iopscience.iop.org/article/10.1209/epl/i2002-00274-6>
- Starostin, V., Pithan, L., Greco, A., Munteanu, V., Gerlach, A., Hinderhofer, A. & Schreiber, F. (2022). *Synchrotron Radiation News*, **35**(4), 21–27.
 10.1080/08940886.2022.2112499
- Suzuki, Y., Hino, H., Hawai, T., Saito, K., Kotsugi, M. & Ono, K. (2020). *Scientific Reports*, **10**(1), 21790.
 10.1038/s41598-020-77474-4
- Szymanski, N. J., Bartel, C. J., Zeng, Y., Diallo, M., Kim, H. & Ceder, G. (2023). *npj Computational Materials*, **9**(1), 31.
 10.1038/s41524-023-00984-y
- Tango (2023). Tango Controls.
<https://www.tango-controls.org/>
- Tolan, M. (1999). *X-ray scattering from soft-matter thin films: materials science and basic research*. No. 148 in Springer tracts in modern physics. Berlin ; New York: Springer.
- Treece, B. W., Kienzle, P. A., Hoogerheide, D. P., Majkrzak, C. F., Lösche, M. & Heinrich, F. (2019). *Journal of Applied Crystallography*, **52**(1), 47–59.
 10.1107/S1600576718017016

- Visa (2023). VISA - Virtual Infrastructure for Scientific Analysis.
<https://visa.readthedocs.io>
- Wilkinson, M. D., Dumontier, M., Aalbersberg, I. J., Appleton, G., Axton, M., Baak, A., Blomberg, N., Boiten, J.-W., Da Silva Santos, L. B., Bourne, P. E., Bouwman, J., Brookes, A. J., Clark, T., Crosas, M., Dillo, I., Dumon, O., Edmunds, S., Evelo, C. T., Finkers, R., Gonzalez-Beltran, A., Gray, A. J., Groth, P., Goble, C., Grethe, J. S., Heringa, J., T Hoen, P. A., Hooft, R., Kuhn, T., Kok, R., Kok, J., Lusher, S. J., Martone, M. E., Mons, A., Packer, A. L., Persson, B., Rocca-Serra, P., Roos, M., Van Schaik, R., Sansone, S.-A., Schultes, E., Sengstag, T., Slater, T., Strawn, G., Swertz, M. A., Thompson, M., Van Der Lei, J., Van Mulligen, E., Velterop, J., Waagmeester, A., Wittenburg, P., Wolstencroft, K., Zhao, J. & Mons, B. (2016). *Scientific Data*, **3**(1), 160018.
10.1038/sdata.2016.18
- Witte, G. & Wöll, C. (2004). *Journal of Materials Research*, **19**(7), 1889–1916.
10.1557/JMR.2004.0251
- Yager, K. G., Majewski, P. W., Noack, M. M. & Fukuto, M. (2023). *Nanotechnology*, **34**(32), 322001.
10.1088/1361-6528/acd25a
- Yanxon, H., Weng, J., Parraga, H., Xu, W., Ruett, U. & Schwarz, N. (2023). *Journal of Synchrotron Radiation*, **30**(1), 137–146.
10.1107/S1600577522011274
- Zhao, Z., Chavez, T., Holman, E. A., Hao, G., Green, A., Krishnan, H., McReynolds, D., Pandolfi, R., Roberts, E. J., Zwart, P. H., Yanxon, H., Schwarz, N., Sankaranarayanan, S., Kalinin, S. V., Mehta, A., Campbell, S. & Hexemer, A. (2022). Publisher: arXiv. DOI: 10.48550/ARXIV.2208.09751.
<https://arxiv.org/abs/2208.09751>
- Zykov, A., Bommel, S., Wolf, C., Pithan, L., Weber, C., Beyer, P., Santoro, G., Rabe, J. P. & Kowarik, S. (2017). *The Journal of Chemical Physics*, **146**(5), 052803.
10.1063/1.4961460

Supporting Information - Closing the loop: Autonomous experiments enabled by machine-learning-based online data analysis in synchrotron beamline environments

LINUS PITHAN,^{a*} VLADIMIR STAROSTIN,^a DAVID MARECEK,^b
LUKAS PETERSDORF,^c CONSTANTIN VÖLTER,^a VALENTIN MUNTEANU,^a
MACIEJ JANKOWSKI,^d OLEG KONOVALOV,^d ALEXANDER GERLACH,^a
ALEXANDER HINDERHOFER,^a BRIDGET MURPHY,^c STEFAN KOWARIK^{b*} AND
FRANK SCHREIBER ^{a*}

^a*Universität Tübingen, Inst. für Angewandte Physik, Auf der Morgenstelle 10, 72076 Tübingen, Germany,* ^b*Universität Graz, Physikalische und Theoretische Chemie, Heinrichstraße 28, 8010 Graz, Austria,* ^c*Universität Kiel, Inst. für Experimentelle und Angewandte Physik, Leibnizstraße 19, 24118 Kiel, Germany,* and ^d*ESRF, The European Synchrotron, 71 avenue des Martyrs, CS 40220, 38043 Grenoble Cedex 9, France . E-mail: linus.pithan@uni-tuebingen.de, stefan.kowarik@uni-graz.at, frank.schreiber@uni-tuebingen.de*

machine learning; reflectometry; xrr; nr; synchrotron; autonomous experiments; closed loop control;

beamline control

At the time of the experiment BLISS 1.10 and pytango 9.3 were available on the ID10 beamline.

SI-1. Tango device servers wrapping around ML Models

A tango device server with specific API to wrap around the ML models developed based on pytorch and tensorflow used in the context of this study.

```

1 from typing import Iterable
2 import numpy as np
3 from pprint import pprint
4
5 from tango.server import Device
6 from tango.server import run
7 from tango.server import attribute, command, device_property
8 from tango import AttrWriteType
9
10 # python code wrapping around pytorch model
11 # available on request or in follow-up publication
12 from reflectorch.inference import InferenceModel
13
14
15 def energy_to_wavelength(energy: float):
16     """Conversion from photon energy (eV) to photon wavelength (
17     angstroms)"""
18     return 1.2398 / energy * 1e4
19
20 class TorchEvaluator(Device):
21     preprocess_attributes = {
22         "beam_width": np.float64,
23         "sample_length": np.float64,
24         "energy_keV": np.float64,
25     }
26
27     input_attributes = {
28         "tth": [np.float64],
29         "intensity": [np.float64],
30         "transm": [np.float64],
31         "priors": [[np.float64]],
32         "count_time": [np.float64],
33     }
34     prediction_attributes = {
35         "q": [np.float64],
36         "q_interp": [np.float64],
37         "refl": [np.float64],
38         "refl_interp": [np.float64],
39         "refl_predicted": [np.float64],
40         "refl_predicted_polished": [np.float64],
41         "parameters": [np.float64],
42         "parameters_polished": [np.float64],
43         "parameter_names": [str],

```

```

44     "sld_profile": [np.float64],
45     "sld_x_axis": [np.float64],
46     "sld_profile_polished": [np.float64],
47 }
48
49 def __init__(self, *args, **kwargs):
50     Device.__init__(self, *args, **kwargs)
51
52     self._prefix_dict = dict()
53
54     self._input_data = self._initialize_dynamic_attributes(
55         "input", self.input_attributes
56     )
57     self._prediction_output = self._initialize_dynamic_attributes(
58         "prediction", self.prediction_attributes
59     )
60     self._preprocess_data = self._initialize_dynamic_attributes(
61         "preprocess", self.preprocess_attributes
62     )
63     self.inference_model = InferenceModel("l2q256_exp_3")
64
65     @property
66     def prediction_output(self):
67         return self._prediction_output
68
69     @command(dtype_out=int)
70     def predict(self) -> dict:
71         """
72         blocking command that runs pytorch model inference
73         """
74         intensity = self._input_data["intensity"]
75         scattering_angle = self._input_data["tth"]
76         attenuation = self._input_data["transm"]
77         priors = self._input_data["priors"]
78
79         preprocess_params = {
80             "wavelength": energy_to_wavelength(
81                 self._preprocess_data["energy_keV"] * 1000
82             ),
83             "beam_width": self._preprocess_data["beam_width"],
84             "sample_length": self._preprocess_data["sample_length"],
85         }
86
87         self.inference_model.set_preprocessing_parameters(**
88             preprocess_params)
89
90         res_dict = self.inference_model.predict(
91             intensity, scattering_angle, attenuation, priors,
92         )
93
94         pprint(res_dict)
95
96         self.prediction_output["q"] = res_dict["q_values"]
97         self.prediction_output["q_interp"] = res_dict["q_interp"]
98         self.prediction_output["refl"] = res_dict["curve"]
99         self.prediction_output["refl_interp"] = res_dict["curve_interp"]

```

```

]
99     self.prediction_output["refl_predicted"] = res_dict["
curve_predicted"]
100     self.prediction_output["parameters"] = res_dict["params"]
101     self.prediction_output["sld_profile"] = res_dict["sld_profile"]
102     self.prediction_output["sld_x_axis"] = res_dict["sld_x_axis"]
103     self.prediction_output["parameter_names"] = res_dict["
param_names"]
104
105     self.prediction_output["refl_predicted_polished"] = res_dict["
curve_polished"]
106     self.prediction_output["parameters_polished"] = res_dict["
params_polished"]
107     self.prediction_output["sld_profile_polished"] = res_dict[
108         "sld_profile_polished"
109     ]
110
111     return 0
112
113     def _initialize_dynamic_attributes(self, prefix, attributes):
114         """
115         boiler plate code to achieve generic handling of data arrays
and
116         parameters that have to be passed into the tango server and
back
117         to the client
118         """
119
120         if prefix in self._prefix_dict:
121             att_dict = self._prefix_dict[prefix]
122         else:
123             att_dict = dict()
124
125         for k, v in attributes.items():
126             att_type = None
127
128             if isinstance(v, tuple):
129                 att_type = v[0]
130                 att_dict[k] = v[1]
131             elif isinstance(v, Iterable):
132                 att_type = v
133                 att_dict[k] = []
134             else:
135                 att_type = v
136                 att_dict[k] = None
137
138             attr = attribute(
139                 name=prefix + "_" + k,
140                 dtype=att_type,
141                 access=AttrWriteType.READ_WRITE,
142                 fget=self._generic_read,
143                 fset=self._generic_write,
144                 max_dim_x=256, # self.N_MAX_X,
145                 max_dim_y=256, # self.N_MAX_Y,
146                 # fisallowed=self.generic_is_allowed,
147             )

```

```

148         self.add_attribute(attr)
149
150         self._prefix_dict[prefix] = att_dict
151         return self._prefix_dict[prefix]
152
153     def _generic_read(self, attr):
154         prefix, name = attr.get_name().split("_", 1)
155         value = self._prefix_dict[prefix][name]
156         # unlike a normal static attribute read, one has to modify the
157         # value
158         # inside this attr object, rather than just returning the value
159         attr.set_value(value)
160
161     def _generic_write(self, attr):
162         prefix, name = attr.get_name().split("_", 1)
163         self._prefix_dict[prefix][name] = attr.get_write_value()
164
165 if __name__ == "__main__":
166     run((TorchEvaluator,))

```

SI-2. Beamline / BLISS integration to run ML inference on remote tango device server and publish prediction results together with raw data

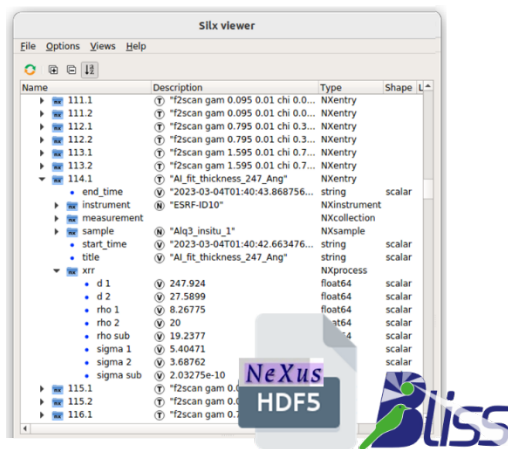


Fig. SI-1.: NeXus compliant data file generated by the beamline control system including results of the online data analysis.

Script that can be loaded as BLISS user macro into the beamline software environment without any additional external dependencies. The function `predict_and_save` takes a bliss scan object as input, runs ML inference and processes the results so that they are saved together with the raw data in a coherent fashion.

References:

https://bliss.gitlab-pages.esrf.fr/bliss/1.10.x/scan_group.html#sequences

(accessed: 05.2023)

[https://bliss.gitlab-pages.esrf.fr/bliss/1.10.x/data/data_scan_metadata.](https://bliss.gitlab-pages.esrf.fr/bliss/1.10.x/data/data_scan_metadata.html)

html (accessed: 05.2023)

```

1 import numpy as np
2 from dataclasses import dataclass
3
4 from bliss.common import tango
5 from bliss import setup_globals
6 from bliss.scanning.group import Sequence
7 from bliss.scanning.chain import AcquisitionChannel
8 from bliss.scanning.scan_meta import USER_SCAN_META
9
10 # Add XRR Metadata entry to BLISS
11 if "xrr" not in USER_SCAN_META.categories_names():
12     USER_SCAN_META.add_categories({"xrr"})
13     USER_SCAN_META.xrr.set("xrr", {"@NX_class": "NXprocess"})
14
15
16 @dataclass
17 class Priors:
18     d_top: tuple = (0.0, 1000.0)
19     d_sio2: tuple = (10.0, 30.0)
20
21     sigma_top: tuple = (0.0, 50.0)
22     sigma_sio2: tuple = (
23         0.0,
24         10.0,
25     )
26     sigma_si: tuple = (
27         0.0,
28         2.0,
29     )
30
31     rho_top: tuple = (7.0, 14.0)
32     rho_sio2: tuple = (19, 23)
33     rho_si: tuple = (19, 21)
34     max_d_change: float = 5.0
35     fit_growth: bool = True
36
37     def to_arr(self):
38         return np.array(
39             [
40                 self.d_top,
41                 self.d_sio2,
42                 self.sigma_top,
43                 self.sigma_sio2,
44                 self.sigma_si,

```

```

45         self.rho_top,
46         self.rho_sio2,
47         self.rho_si,
48     ]
49     )
50
51
52 @dataclass
53 class PreprocessParams:
54     energy_keV: float = 17.0
55     beam_width: float = 0.03
56     sample_length: float = 9.0
57
58
59 def predict_and_save(
60     scans, priors=None, preprocess: PreprocessParams = None,
61 ):
62     """
63     takes a list of scans that will be concatenated to a single XRR
64     profile,
65     performs basic background correction, pushes data via TANGO into
66     the ML model,
67     triggers inference in the TANGO device, retrieves prediction
68     results and
69     publishes results via BLISS to be saved together with original
70     scans in
71     the NeXus hdf5 file produced by the BLISS NeXusWriter
72     """
73
74     # specify the tango uri of the device server embedding the ML-Model
75     tango_uri_or_proxy = ("//VISA-HOST.esrf.fr:PORT/PATH/TO/TANGO-ML-
76     DEVICE",)
77
78     # specify counters that should be used to collect the data from the
79     scan object
80     TTH = setup_globals.gam # gam: angle of detector axis
81     CROI = "pilatus300k:roi_counters:roi2_sum" # ROI with specular
82     signal
83     BGROI1 = (
84         "pilatus300k:roi_counters:roi3_sum" # ROI left of CROI (half
85         the size of CROI)
86     )
87     BGROI2 = (
88         "pilatus300k:roi_counters:roi4_sum" # ROI right of CROI (half
89         the size of CROI)
90     )
91     TRANSM = "autof_eh1:transm" # transmission of Autoabsorber
92
93     # extract detector angle from scans
94     tth_data = np.concatenate(np.array([x.get_data(TTH) for x in scans
95     ]))
96
97     # extract transmission of attenuators from scans
98     transm_data = np.concatenate(np.array([x.get_data(TRANSM) for x in
99     scans]))

```

```

90 # extract measured intensities from scans and perform basic
background correction
91 intens_data = np.concatenate(
92     np.array(
93         [x.get_data(CROI) - x.get_data(BGROI1) - x.get_data(BGROI2)
94         for x in scans]
95     )
96 )
97 # establish communication with tango device that is linked to ML
model
98 ml_device = tango.DeviceProxy(tango_uri_or_proxy)
99
100 # deal with priors and preprocessing parameters
101 priors = priors or Priors()
102 preprocess = preprocess or PreprocessParams()
103
104 # push data to tango device
105 ml_device.input_tth = tth_data
106 ml_device.input_transm = transm_data
107 ml_device.input_intensity = np.clip(intens_data, 0, np.infty)
108 ml_device.input_count_time = [0]
109 ml_device.input_priors = priors.to_arr()
110 ml_device.postprocess_max_d_change = priors.max_d_change
111 ml_device.postprocess_fit_growth = priors.fit_growth
112 ml_device.preprocess_beam_width = preprocess.beam_width
113 ml_device.preprocess_sample_length = preprocess.sample_length
114 ml_device.preprocess_energy_keV = preprocess.energy_keV
115
116 # run inference (here built to run synchronous in blocking fashion)
117 ml_device.set_timeout_millis(5000)
118 ml_device.predict()
119
120 # retrieve predicted parameters
121 # polished parameters refers to results of subsequent LMS fit after
inference
122 polished_params = ml_device.prediction_parameters_polished
123 param_names = ml_device.prediction_parameter_names
124
125 # create summary metadata structure that is to be published via
BLISS
126 info = {"xrr": dict(zip(param_names, polished_params))}
127
128 # creates a new entry in the hdf5 file generated by BLISS and redis
DB for online access
129 seq = Sequence(
130     title=f"AI_fit_thickness_{int(polished_params[0])}_Ang",
scan_info=info
131 )
132
133 # specify additional data entries that should appear under "
measurement" in the h5 file
134 seq.add_custom_channel(AcquisitionChannel("raw_tth", float, ()))
135 seq.add_custom_channel(AcquisitionChannel("corrected_intensity",
float, ()))
136 seq.add_custom_channel(AcquisitionChannel("raw_q", float, ()))

```

```

137     seq.add_custom_channel(AcquisitionChannel("predicted_intensity",
138     float, ()))
139     seq.add_custom_channel(AcquisitionChannel("predicted_q", float, ()))
140     seq.add_custom_channel(AcquisitionChannel("params", float, ()))
141     seq.add_custom_channel(AcquisitionChannel("params_names", str, ()))
142     seq.add_custom_channel(AcquisitionChannel("polished_intensity",
143     float, ()))
144     seq.add_custom_channel(AcquisitionChannel("polished_params", float,
145     ()))
146
147     # add references to the raw data scans as well as process data and
148     # analysis results
149     with seq.sequence_context() as scan_seq:
150         for scan in scans:
151             scan_seq.add(scan)
152
153             seq.custom_channels["raw_tth"].emit(tth_data)
154             seq.custom_channels["corrected_intensity"].emit(ml_device.
155             prediction_refl)
156             seq.custom_channels["raw_q"].emit(ml_device.prediction_q)
157             seq.custom_channels["predicted_intensity"].emit(
158             ml_device.prediction_refl_predicted
159             )
160             seq.custom_channels["params"].emit(ml_device.
161             prediction_parameters)
162             seq.custom_channels["params_names"].emit(ml_device.
163             prediction_parameter_names)
164             seq.custom_channels["polished_intensity"].emit(
165             ml_device.prediction_refl_predicted_polished
166             )
167             seq.custom_channels["polished_params"].emit(polished_params)
168
169     # return polished_params e.g. for closed loop feedback
170     return polished_params

```

SI-3. Asynchronous BLISS integration to receive events via the BLISS data streaming API

The code snippet below represents basically a consumer of events emitted via the event based data streaming api of BLISS and publishes produced results using a beacon channel.

References: https://bliss.gitlab-pages.esrf.fr/bliss/1.10.x/data/data_redis_api_low.html (accessed: 05.2023)

https://bliss.gitlab-pages.esrf.fr/bliss/1.10.x/beacon_channels.html (accessed: 05.2023)

```

1 from bliss.data.node import get_session_node
2 from bliss.config.channels import Channel
3
4 # create BLISS Channel with unique name in the scope of the beamline
5 # to publish predictions results via beacon / redis
6 last_film_thickness = Channel("last_film_thickness", default_value=None
7 )
8
9 def listen_scans_of_session(session):
10     """
11     script that can run in any bliss process
12     (independent of the process producing the data & controlling the
13     hardware)
14     takes as input argument the name of the bliss session publishing
15     the data
16     to the beamline beacon server / redis
17     """
18     session_node = get_session_node(session)
19     print(f"Listening to {session}")
20
21     received_scans = []
22     for event_type, node, event_data in session_node.walk_on_new_events
23     (
24         include_filter=["scan"]
25     ):
26         # this loop deals with the event based data streaming api of
27         BLISS
28         #
29         if event_type == event_type.NEW_NODE:
30             print(f"new scan", node.db_name)
31
32         elif event_type == event_type.END_SCAN:
33             print(node.db_name)
34
35             params = node.info.get("fastfit")
36             if params.get("xrr_scan_group_first", False):
37                 received_scans = [node]
38                 print("add scan")
39             if params.get("xrr_scan_group_last", False):
40                 received_scans.append(node)
41                 print("add scan and process")
42                 process_scans(received_scans)
43
44 def process_scans(scans):
45     """
46     Run ML inference
47     """
48
49     # missing here: code similar to synchronous version in example
50     above
51     # interacting with tango or triton server to retrieve prediction
52     # ...

```

```

51 thickness = prediction["parameters_polished"][0]
52
53 # publish e.g. film thickness via bliss channel & beacon
54 # to make it available to all bliss processes running on the
55 # beamline
56 last_film_thickness.value = thickness
57
58 print("##### predicted thickness", thickness)

```

SI-4. Postprocessing gradient-descent fit with optional growth rate parameter.

The functions below are used to perform a postprocessing polishing operation by fitting the measured curve via gradient descent initialized based on AI result. Optionally, it allows fitting the linear change of the thickness of the top layer as a function of q for curves measured *in situ* during growth. Further details may be found in (Munteanu *et al.*, 2023).

References:

Munteanu, V., Starostin, V., Greco, A., Pithan, L., Gerlach, A., Hinderhofer, A., Kowarik, S. Schreiber, F. (2023). Neural network analysis of neutron and X-ray reflectivity data: incorporating prior knowledge for tackling the phase problem.

```

1 import numpy as np
2 from scipy.optimize import minimize, curve_fit
3
4 def abeles_np(
5     q: np.ndarray,
6     thickness: np.ndarray,
7     roughness: np.ndarray,
8     sld: np.ndarray):
9
10    c_dtype = np.complex128 if q.dtype is np.float64 else np.complex64
11
12    if q.ndim == thickness.ndim == roughness.ndim == sld.ndim == 1:
13        zero_batch = True
14    else:
15        zero_batch = False
16

```

```

17 thickness = np.atleast_2d(thickness)
18 roughness = np.atleast_2d(roughness)
19 sld = np.atleast_2d(sld)
20 batch_size, num_layers = thickness.shape
21 sld = np.concatenate([np.zeros((batch_size, 1)).astype(sld.dtype),
sld], -1)[: , None]
22 thickness = np.concatenate([np.zeros((batch_size, 1)).astype(
thickness.dtype), thickness], -1)[: , None]
23 roughness = roughness[: , None] ** 2
24
25 sld = sld * 1e-6 + 1e-30j
26
27 k_z0 = (q / 2).astype(c_dtype)
28 if len(k_z0.shape) == 1:
29     k_z0 = k_z0[None]
30 if len(k_z0.shape) == 2:
31     k_z0 = k_z0[... , None]
32 k_n = np.sqrt(k_z0 ** 2 - 4 * np.pi * sld)
33 k_n, k_np1 = k_n[... , :-1], k_n[... , 1:]
34
35 beta = 1j * thickness * k_n
36
37 exp_beta = np.exp(beta)
38 exp_m_beta = np.exp(-beta)
39 rn = (k_n - k_np1) / (k_n + k_np1) * np.exp(- 2 * k_n * k_np1 *
roughness)
40
41 c_matrices = np.stack([
42     np.stack([exp_beta, rn * exp_m_beta], -1),
43     np.stack([rn * exp_beta, exp_m_beta], -1),
44 ], -1)
45 c_matrices = np.moveaxis(c_matrices, -3, 0)
46 m, c_matrices = c_matrices[0], c_matrices[1:]
47 for c in c_matrices:
48     m = m @ c
49
50 r = np.abs(m[... , 1, 0] / m[... , 0, 0]) ** 2
51 r = np.clip(r, None, 1.)
52
53 if zero_batch:
54     r = r[0]
55 return r
56
57
58 def standard_restore_params(fitted_params) -> dict:
59     num_layers = (fitted_params.size - 2) // 3
60     return dict(
61         thickness=fitted_params[:num_layers],
62         roughness=fitted_params[num_layers:2 * num_layers + 1],
63         sld=fitted_params[2 * num_layers + 1:],
64     )
65
66
67 def mse_loss(curve1, curve2):
68     return np.sum((curve1 - curve2) ** 2)
69

```

```

70
71 def standard_refl_fit(
72     q: np.ndarray, curve: np.ndarray,
73     init_params: np.ndarray,
74     bounds: np.ndarray = None,
75     refl_generator=abeles_np,
76     restore_params_func=standard_restore_params,
77     scale_curve_func=np.log10,
78     **kwargs):
79
80     if bounds is not None:
81         kwargs['bounds'] = bounds
82         init_params = np.clip(init_params, *bounds)
83
84     res = curve_fit(
85         get_scaled_curve_func(
86             refl_generator=refl_generator,
87             restore_params_func=restore_params_func,
88             scale_curve_func=scale_curve_func,
89         ),
90         q, scale_curve_func(curve),
91         p0=init_params, **kwargs
92     )
93
94     curve = refl_generator(q, **restore_params_func(res[0]))
95     return res[0], curve
96
97
98 def get_fit_with_growth(
99     q: np.ndarray, curve: np.ndarray,
100     init_params: np.ndarray,
101     bounds: np.ndarray = None,
102     init_d_change: float = 0.,
103     max_d_change: float = 30.,
104     scale_curve_func=np.log10,
105     **kwargs):
106
107     init_params = np.array(list(init_params) + [init_d_change])
108     if bounds is not None:
109         bounds = np.concatenate([bounds, np.array([0, max_d_change])
110     [..., None]], -1)
111
112     params, curve = standard_refl_fit(
113         q, curve, init_params, bounds, refl_generator=
114         refl_with_changing_params,
115         restore_params_func=get_restore_params_with_growth_func(q_size=
116         q.size, d_idx=0),
117         scale_curve_func=scale_curve_func, **kwargs
118     )
119     params[0] += params[-1] / 2
120     return params, curve
121
122 def fit_refl_curve(q: np.ndarray, curve: np.ndarray,
123     init_params: np.ndarray,
124     bounds: np.ndarray = None,

```



```

123         refl_generator=abeles_np,
124         restore_params_func=standard_restore_params,
125         scale_curve_func=np.log10,
126         **kwargs
127     ) -> np.ndarray
128
129     fitting_func = get_fitting_func(
130         q=q, curve=curve,
131         refl_generator=refl_generator,
132         restore_params_func=restore_params_func,
133         scale_curve_func=scale_curve_func,
134     )
135
136     res = minimize(fitting_func, init_params, bounds=bounds, **kwargs)
137
138     if not res.success:
139         import warnings
140         warnings.warn(f"Minimization did not converge.")
141     return res.x
142
143
144 def get_scaled_curve_func(
145     refl_generator=abeles_np,
146     restore_params_func=standard_restore_params,
147     scale_curve_func=np.log10):
148
149     def scaled_curve_func(q, *fitted_params):
150         fitted_params = restore_params_func(np.asarray(fitted_params))
151         fitted_curve = refl_generator(q, **fitted_params)
152         scaled_curve = scale_curve_func(fitted_curve)
153         return scaled_curve
154
155     return scaled_curve_func
156
157
158 def get_fitting_func(
159     q: np.ndarray,
160     curve: np.ndarray,
161     refl_generator=abeles_np,
162     restore_params_func=standard_restore_params,
163     scale_curve_func=np.log10,
164     loss_func=mse_loss):
165
166     scaled_curve = scale_curve_func(curve)
167
168     def fitting_func(fitted_params):
169         fitted_params = restore_params_func(fitted_params)
170         fitted_curve = refl_generator(q, **fitted_params)
171         loss = loss_func(scale_curve_func(fitted_curve), scaled_curve)
172         return loss
173
174     return fitting_func
175
176
177 def restore_masked_params(fixed_params, fixed_mask):
178     def restore_params(fitted_params) -> dict:

```

```

179     params = np.empty_like(fixed_mask).astype(fitted_params.dtype)
180     params[fixed_mask] = fixed_params
181     params[~fixed_mask] = fitted_params
182     return standard_restore_params(params)
183
184     return restore_params
185
186
187 def base_params2growth(base_params: dict, d_shift: np.ndarray, d_idx:
188 int = 0) -> dict:
189     d_init = base_params['thickness'][None]
190     q_size = d_shift.size
191     d = d_init.repeat(q_size, 0)
192     d[:, d_idx] = d[:, d_idx] + d_shift
193
194     roughness = np.broadcast_to(base_params['roughness'][None], (q_size
195 , base_params['roughness'].size))
196     sld = np.broadcast_to(base_params['sld'][None], (q_size,
197 base_params['sld'].size))
198
199     return {
200         'thickness': d,
201         'roughness': roughness,
202         'sld': sld,
203     }
204
205 def get_restore_params_with_growth_func(q_size: int, d_idx: int = 0):
206     def restore_params_with_growth(fitted_params) -> dict:
207         fitted_params, delta_d = fitted_params[:-1], fitted_params[-1]
208         base_params = standard_restore_params(fitted_params)
209         d_shift = np.linspace(0, delta_d, q_size)
210         return base_params2growth(base_params, d_shift, d_idx)
211
212     return restore_params_with_growth
213
214 def refl_with_changing_params(q: np.ndarray, **kwargs):
215     return abeles_np(q[...], None, **kwargs).flatten()

```